Check for updates

Structural, optical, electric and dielectric characterization of a $NaCu_{0.2}Fe_{0.3}Mn_{0.5}O_2$ compound

Ichrak Ben Slima,[a] Karim Karoui, [iD] [a] Abdelfattah Mahmoud, [iD] [b] Frédéric Boschini[b] and Abdallah Ben Rhaiem [iD] *[a]

The compound $NaCu_{0.2}Fe_{0.3}Mn_{0.5}O_2$ was synthesized using a solid-state method and it crystallized in a hexagonal system with a $R\bar{3}m$ space group in an O3-type phase. The optical properties were measured using UV-Vis absorption spectrometry to determine the absorption coefficient α and the optical band gap E_g. The optical band gap energy of this sample is 2.45 eV, which indicates that it has semiconductor characteristics. Furthermore, the electrical and dielectric properties of the material were investigated using complex impedance spectroscopy between 10^{-1} Hz and 10^6 Hz at various temperatures (333–453 K). The permittivity results prove that there are two types of polarization, dipolar polarization and space charge polarization. The Nyquist diagrams show the contribution of the effects of the grain, grain boundary, and electrode properties. The frequency dependence of the conductivity was interpreted in terms of Jonscher's law. The DC conductivity follows both the Mott and Arrhenius laws at low and high temperature, respectively. The temperature dependence of the power law exponent(s) suggests that the overlapping large polaron tunneling (OLPT) model is the dominant transport process in this material. The optimum hopping length of the polaron (4 Å) is large compared with the interatomic spacing (2.384 Å for Na–O and 2.011 Å for Cu, Fe, Mn–O).

1. Introduction

The Na_xMO_2 ternary oxides, where M is a 3d transition metal (Co, Cr, Fe, Mn, V, and their combinations), are used as positive electrodes for sodium ion batteries because of their simple structure, easy of synthesis, environmental friendliness, high exploitation potential and feasibility of commercial production.[1] Furthermore, those oxides have not only important electrochemical properties but also exhibit various interesting physical properties.

However, these electrode compounds are characterized by a layered framework structure in which the sodium ion layers (Na^+) are intercalated between two MO_2 sheets. The arrangement of these sheets determines the type of structure of the sample, and the MO_2 sheets are formed either by MO_6 octahedrons in the 'O' structure, where Na^+ occupy an octahedral site, or by MO_4 polyhedrons in the 'P' structure, where Na^+ occupy a prismatic site.[2] This type of structure influences the electrical properties of these compounds, in particular the electrical conductivity because the charge carrier, Na^+, is free to move. In addition, to the band gap between the valence band and the

conduction band, which indicates the semiconductor comportment, the 3d transition metals, are characterized by the overlap between the narrow 3d bands.[3]

In this study, there was interest in the combination between Cu, Fe and Mn due to their abundant resources, inexpensive price and because they are harmless to the environment.[4–6] Furthermore, the compound $O3-Na_{0.9}[Cu_{0.22}Fe_{0.30}Mn_{0.48}]O_2$ shows interesting electrochemistry results such as: an energy density equal to 210 W h kg^{-1}, a 90% round-trip energy efficiency and good cycling stability.[7]

These results encouraged the investigation and study of the $NaCu_{0.2}Fe_{0.3}Mn_{0.5}O_2$ compound. Firstly, a structural study using X-ray diffraction (XRD) at room temperature is reported. Then, the band gap and Urbach energies obtained from the absorbance spectra of UV-visible (UV-Vis) spectroscopy, at ambient temperature were investigated. Finally, the complex impedance spectroscopy measurements were performed, in the temperature and frequency ranges of 333–453 K and 10^{-1} to 10^6 Hz, respectively, which were used to determine the electric and dielectric properties.

2. Materials and methods

The $NaCu_{0.2}Fe_{0.3}Mn_{0.5}O_2$ compound was synthesized using a solid-state reaction. The precursors, of Na_2CO_3 (99%), CuO (99%), Fe_2O_3 (99%) and Mn_2O_3 (99%) were obtained from

[a] *Laboratory LaSCOM, University of Sfax, BP1171, 3000, Sfax, Tunisia. E-mail: abdallahrhaiem@yahoo.fr*

[b] *GREENMAT, CESAM, Institute of Chemistry B6, University of Liège, 4000, Liège, Belgium*

Sigma-Aldrich, and were mixed in proportional ratios. The obtained powder was burned at 500 °C for 16 h, and then, the sample was ground, pressed into pellets and transferred to an oven at 850 °C for 24 h.

To determine the purity of the sample, powder XRD was performed using a Bruker D8 Discover with Twin/Twin optics, at room temperature, with Cu Kα radiation ($\lambda = 1.5406$ Å, $10° \leq 2\theta \leq 80°$). To precisely determine the optical properties of the prepared sample, a Shimadzu UV-3101 PC scanning spectrophotometer was used at room temperature, with a wavelength range of 200–800 nm, with a sample pellet of 0.5 mm of diameter. Finally, the electrical property measurements were obtained using complex impedance spectroscopy with a Solartron SI 1260 impedance/gain phase analyzer in the temperature and frequency ranges of 333–453 K and 10^{-1} to 10^6 Hz, respectively, with a sample pellet with a thickness of 1 mm and a diameter of 8 mm.

3. Results and discussion

3.1. Structural properties

The XRD pattern associated with the $NaCu_{0.2}Fe_{0.3}Mn_{0.5}O_2$ compound is shown in Fig. 1. The results of the structural refinement by Rietveld method proved that this sample crystallized in a hexagonal system with a $R\bar{3}m$ space group and the cell unit: $a = 2.9389(1)$ Å, $c = 16.5208(11)$ Å, $\alpha = \beta = 90°$ and $\gamma = 120°$. Yet, the refinement factors, which were the fit criteria, such as reliability factor χ^2, fit factors R_p and R_{wp}, which are shown in Table 1, show small values indicating the perfect conformity between the experimental and theoretical spectra and suggesting the purity of the sample. In addition, these results are in good agreement with those found by Mu *et al.*[7]

Fig. 2 shows the crystalline structure of the prepared sample. It is marked by an alternate arrangement of NaO_2 sheets with those of $CuFeMnO_2$. Here, both of the sodium ions and transition metals are linked to six oxygen atoms which build the NaO_6 and MO_6 octahedra. Thus, the structure is an O3 type where 'O' means that the Na ion occupies an octahedral site and

Table 1 Refinement factors for the $NaCu_{0.2}Fe_{0.3}Mn_{0.5}O_2$ sample

χ^2	R_p	R_{wp}	R_{exp}	Bragg R-factor	RF-factor
4.71	14.5	11.8	5.42	2.728	3.523

'3' indicates the number of sheets of transition metals in a repeated unit of stacking. The $NaCu_{0.2}Fe_{0.3}Mn_{0.5}O_2$ sample has a cell volume of 123.75(1) Å^3 and the interatomic distances are 2.384 Å and 2.011 Å for Na–O and CuFeMn–O, respectively. The atomic coordinates are reported in Table 2.

3.2. Optical properties

The optical properties were obtained from the UV-Vis absorbance spectra measured at room and are displayed in Fig. 3. This spectrum is characterized by a high absorbance in both the ultra-violet and the visible region which means the $NaCu_{0.2}Fe_{0.3}Mn_{0.5}O_2$ compound is a suitable candidate for applications in optoelectronics and photovoltaics.[8,9] The presence of four absorbance peaks at 248 nm, 370 nm, 529 nm and 689 nm are noted. The peak which showed the maximum absorbance was in the UV region at 248 nm and indicated the charges transferring from the valence band to the conduction band.[10] The peaks at 370 nm, 529 nm and 689 nm were associated with the absorption of Mn, Fe and Cu, respectively,.[11–13]

For the determination of the optical gap energy the model proposed by Tauc was used.[14] In the region of high absorption, E_g is related to the absorption coefficient α by the following relationship:

$$\alpha h\nu = B(h\nu - E_g)^r \tag{1}$$

where $\alpha = 2.303 \times A/e$, B is a constant, E_g is the optical gap, and r is a constant describing the nature of the optical transition between the valence band and the conduction band.

Fig. 4 presents the Tauc plot of $(\alpha h\nu)^2$ *versus* $h\nu$. The value of the gap energy can be determined from the intersection of the extrapolation of the linear part of $(\alpha h\nu)^2$ with the energy axis.
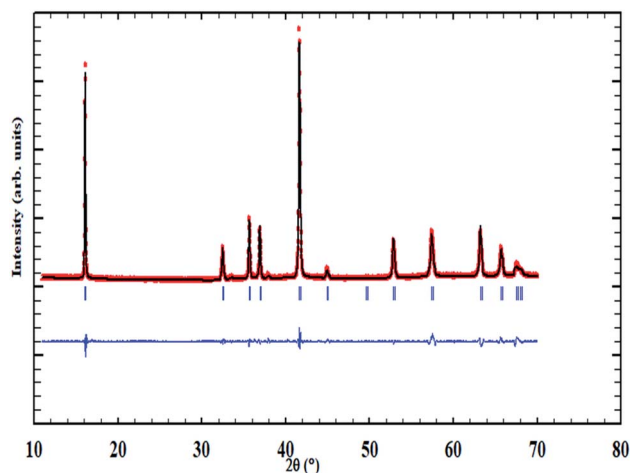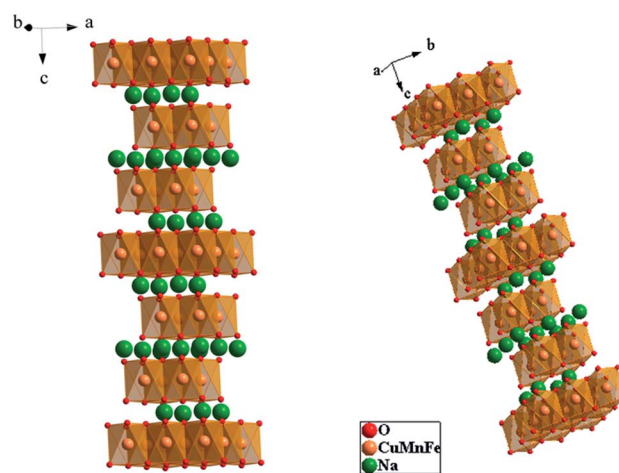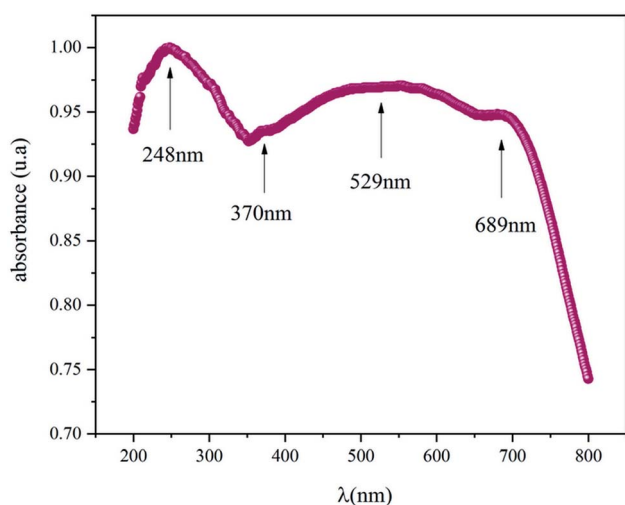

Fig. 1 The XRD pattern of the $NaCu_{0.2}Fe_{0.3}Mn_{0.5}O_2$ sample.

Fig. 2 The crystalline structure of the $NaCu_{0.2}Fe_{0.3}Mn_{0.5}O_2$ sample.

Table 2 The atomic positions of the $NaCu_{0.2}Fe_{0.3}Mn_{0.5}O_2$ sample

Atom	Wyckoff	x (Å)	y (Å)	z (Å)
Na	3b	0	0	0.500
Cu	3a	0	0	0
Fe	3a	0	0	0
Mn	3a	0	0	0
O	6c	0	0	0.268

Fig. 3 The UV-visible absorbance spectrum of the $NaCu_{0.2}Fe_{0.3}Mn_{0.5}O_2$ sample.

The gap energy of the $NaCu_{0.2}Fe_{0.3}Mn_{0.5}O_2$ compound was equal to 2.45 eV which indicated the semiconductor character of this compound. Indeed, the band gap of this sample is smaller than the band gap of $LiCoO_2$, which is widely used as an electrode in lithium-ion batteries, which is 2.7 eV.[15]

The variation of $Ln(\alpha)$ *versus* $(h\nu)$ is plotted in Fig. 5 and it was used to determine the Urbach energy, which describes the disorder of a material, using:[16]

$$\alpha = \alpha_0 \exp\left(\frac{h\nu}{E_u}\right) \qquad (2)$$

where α_0 is a constant, and E_u is the Urbach energy. The Urbach energy was found to be 18.51 eV, which was superior to that of the tail of the bands, previously found in the literature.[17] It was noticed that there was an inverse variation between the optical gap and the disorder. In fact, the gap characterized the energetic difference between the tails of the bands, however the Urbach energy is defined by the width of the tail of the valence bands or conduction band, and therefore an increase in disorder was accompanied by a decrease in the forbidden band.

3.3. Dielectric properties

3.3.1. Dielectric constant. The analysis of the real part of the permittivity and the dielectric loss lead to the investigation
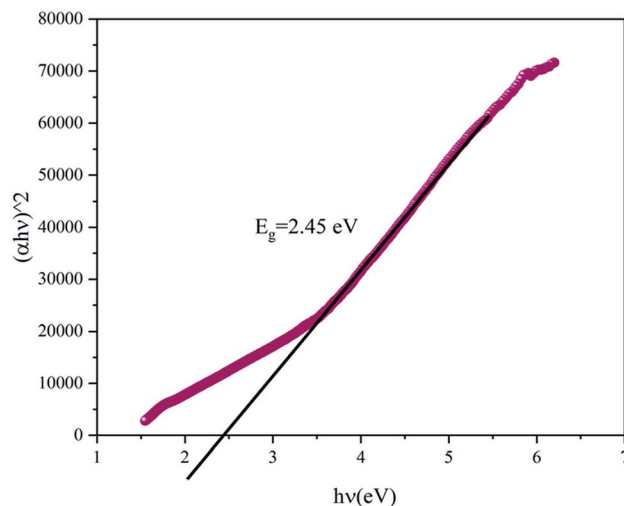
Fig. 4 The Tauc plot of the $NaCu_{0.2}Fe_{0.3}Mn_{0.5}O_2$ sample.

of the phenomenon of polarization in the sample. Fig. 6 shows the evolution of ε' as a function of angular frequency at various temperatures, which was characterized by an exponential decrease. It was clear that ε' showed dispersions at low frequencies, which was verified by the increase of the ε' value to 10^7 as the temperature increased at 1 Hz, and became almost saturated at higher frequencies. This low frequency dielectric dispersion was associated with the effect of the space charge accumulation and/or the movement of the conductive ions. The magnitude of the dielectric constant depended on the degree of polarization and the charge displacement in the crystal. It could be observed that ε' became a constant value at high frequencies, and this was attributed to the absence of space charge polarization near the grain boundary interface. Then, the high dielectric constant in this material ($10^6 < \varepsilon'_{max} < 10^8$), compared to that of Na_2CoSiO_4 ($10 < \varepsilon'_{max} < 10^4$) which was used as battery electrode,[18]
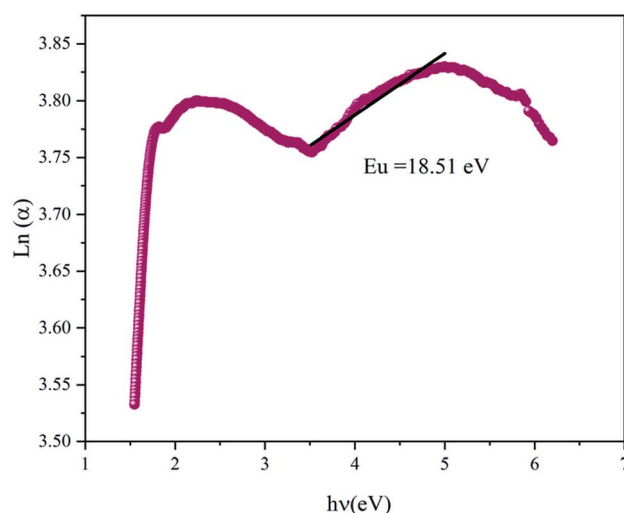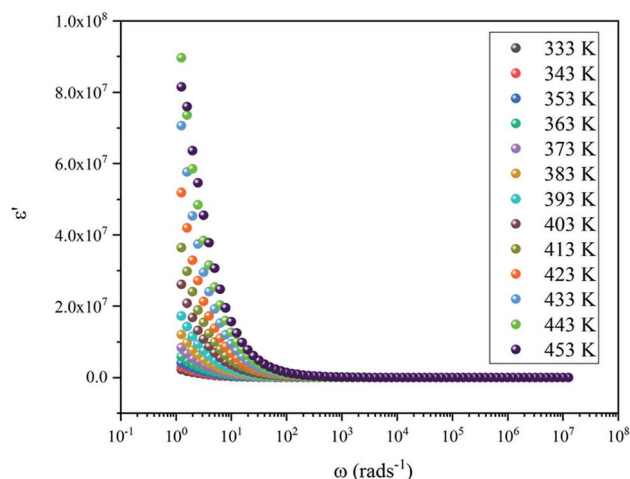

Fig. 5 The variation of $Ln(\alpha)$ *versus* $h\nu$.

Fig. 6 The variation of the real part of the permittivity of the NaCu$_{0.2}$Fe$_{0.3}$Mn$_{0.5}$O$_2$ sample.
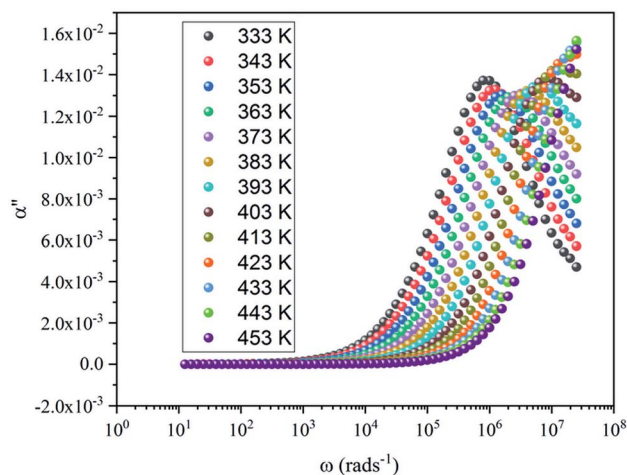

Fig. 7 The imaginary part of complex polarizability as a function of frequency.

implies that this compound could be a candidate for use in energetic devices. Indeed, materials with a large dielectric constant can be used as a dielectric gate or an active channel in field-effect transistor (FET) devices.[19]

3.3.2. Complex polarizability. To understand the phenomena of dielectric relaxation better, the complex polarizability α^*, proposed by Scaife[20] was focused on next. This allows more investigation of the intrinsic dielectric properties of a compound because it gives appropriate weight to all polarization mechanisms. In fact, by using this formalism, diverse, coexisting relaxation processes in a sample could be easily separated. Thus, the complex polarizability is defined as:

$$\alpha^* = \alpha' - i\alpha'' = \frac{(\varepsilon^* + 1)}{(\varepsilon^* + 2)} \tag{3}$$

where α' and α'' are the real and imaginary parts of the complex polarizability (α^*), respectively, and ε^* is the complex dielectric constant. Using the above relationship, the imaginary part of the complex polarizability parameter α'' could be calculated as follows:

$$\alpha'' = \frac{3\varepsilon''}{(\varepsilon' + 2)^2 + \varepsilon''^2} \tag{4}$$

where ε' and ε'' are the real and imaginary parts of the dielectric constant (ε^*), respectively.

Fig. 7 shows the imaginary part of the complex polarizability as a function of frequency at different temperatures. This is characterized by relaxation peaks, defined by a maximum frequency ω_{α_m}, which shifted towards high frequency with the increase of temperature (see Fig. 8). This variation follows the Arrhenius behavior:

$$\omega_\alpha = \omega_{\alpha_0} \exp\left(-\frac{E_a}{KT}\right) \tag{5}$$

where ω_{α_0} is a pre-factor, K is the Boltzmann constant, T is the temperature. and E_a is the activation energy, which is 0.11 eV.

3.3.3. Dielectric loss factor. The dielectric loss factor changes the loss of electrical energy introduced from the movement of the charge carrier and the orientation of dipoles. This can be calculated from:

$$\tan \delta = \frac{\varepsilon''}{\varepsilon'} \tag{6}$$

where ε' and ε'' are the real and imaginary parts of the dielectric constant (ε^*), respectively.

Fig. 9 shows that the relatively low value of tan δ, is about 0–15. It should be noted that, materials with a low energy loss are necessary for battery applications, which means that the NaCu$_{0.2}$Fe$_{0.3}$Mn$_{0.5}$O$_2$ compound is a good candidate for such applications. This also shows two relaxation peaks in a low and a high frequency region, respectively. These peaks were indexed for space charge and dipolar polarization, respectively. With the
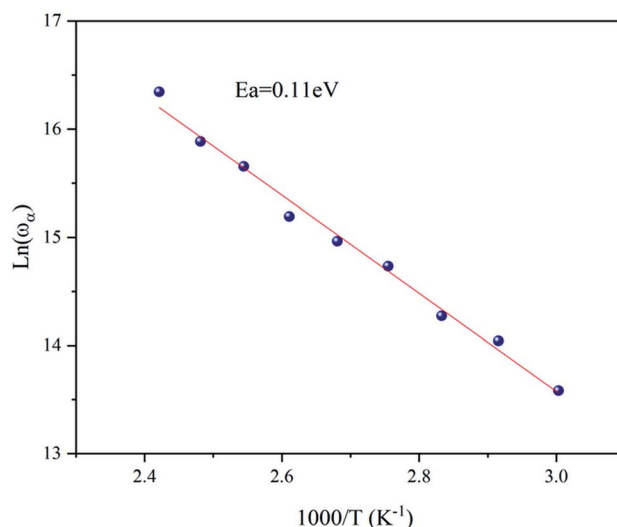

Fig. 8 The variation of Ln(ω_α) versus the inverse of temperature.
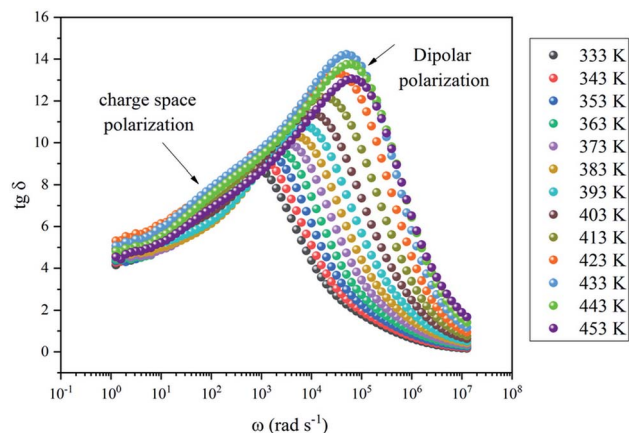
Fig. 9 The variation of the dielectric loss factor at different temperatures.

increase of temperature, the dielectric loss shifts to a higher frequency which indicated that the polarization was thermally activated.

3.4. Electric properties

3.4.1. Impedance spectroscopy. The electric properties were determined from the complex impedance spectroscopy results in the temperature and frequency ranges of 333–453 K and 1–10^6 Hz, respectively. These results were translated using a Nyquist plot: $-Z'' = f(Z')$, as shown in Fig. 10. This plot proved the presence of three semi-circles placed in three frequency domains. In the high frequency this was a grain effect, in the medium frequency it was a grain boundary effect, and in the low frequency it appeared as an electrode effect. These effects were simulated by an equivalent circuit (Fig. 11) using ZView software. This equivalent circuit was formed by three cells in series: the first was formed by a resistance R_g, a capacity C_g and a fractal capacity CPE_g and all were parallel indicating the grain effect, the second was a combination of a resistance R_{gb} in parallel with a fractal capacity CPE_{gb} representing the grain boundary effect,
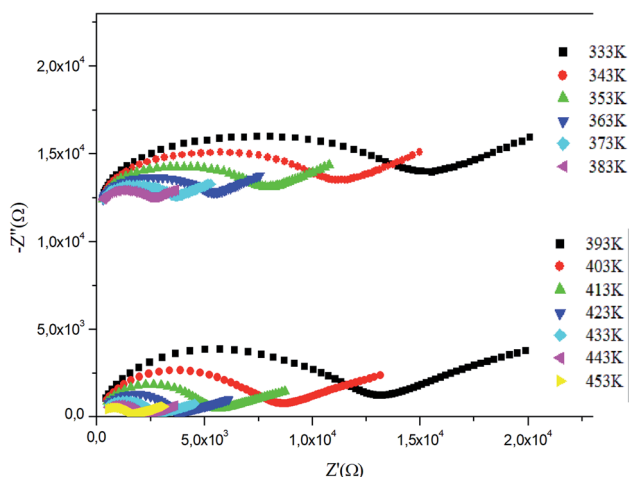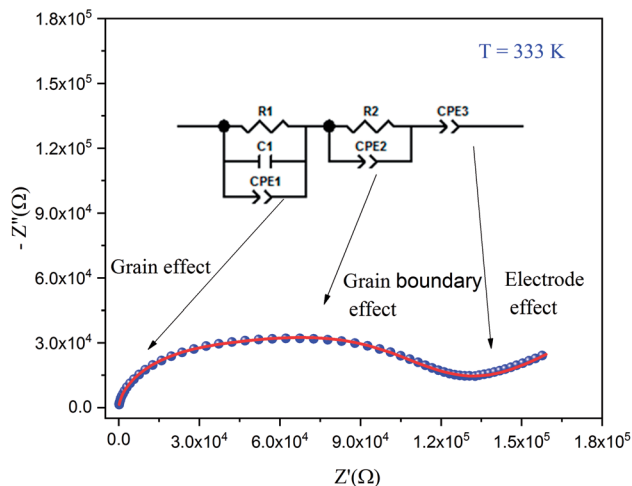

Fig. 11 A simulation of the Nyquist plot at a temperature of 333 K.

and the third one was a fractal capacity CPE_e interpreted as the electrode effect. Fig. 11 shows the simulation of $-Z''$ *versus* Z' at a temperature of 333 K and the effect of each one of the equivalent circuit cells. The intersection of the Nyquist plots with the Z' axes is used to obtain the resistivity of the sample and their values were obtained from the plot simulations with the equivalent circuit. Using the resistivity, the grain conductivity was calculated based on the following relationship:

$$\sigma_g = \frac{e}{R_g S} \tag{7}$$

where: e is the thickness of the pellet, S is the surface area of the pellet, and R_g is the resistance determined from the equivalent circuit.

By increasing in temperature, the resistivity, decreased, which involved the increase of the conductivity of the grain. This means that the conductivity was thermally activated and confirmed the semiconductor behavior of the sample. To understand the variation of the grain conductivity better, Fig. 12
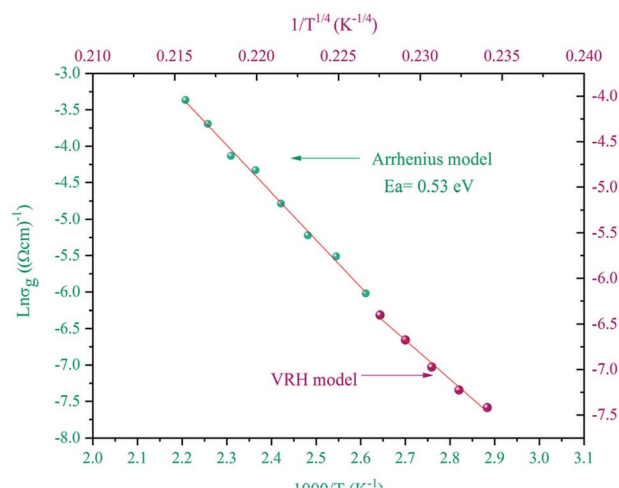

Fig. 10 Nyquist plots of the $NaCu_{0.2}Fe_{0.3}Mn_{0.5}O_2$ compound.

Fig. 12 The variation of the grain conductivity of the $NaCu_{0.2}Fe_{0.3}$-$Mn_{0.5}O_2$ compound.

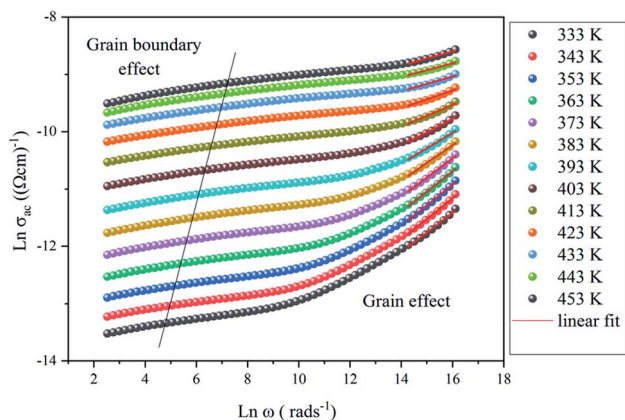**Fig. 13** The variation of $Ln(\sigma_{ac})$ versus $Ln(\omega)$ at different temperatures for the $NaCu_{0.2}Fe_{0.3}Mn_{0.5}O_2$ compound.

Fig. 14 The variation of the exponent S as a function of temperature.

shows $Ln(\sigma_g)$ a function of temperature. It is characterized by the presence of two domains: high and low temperature.

At a high temperature of 383–453 K, all of the charge carriers were thermally active, so, the variation of the grain conductivity followed the Arrhenius law:[21]

$$\sigma_g = \sigma_0 \exp\left(-\frac{E_a}{KT}\right) \qquad (8)$$

where σ_0 is a pre-factor, E_a is the activation energy, K the Boltzmann constant and T is the temperature. The activation energy of this conductivity was equal to 0.53 eV and $\sigma_0 = 4.97 \times 10^{-2}\ \Omega^{-1}\ cm^{-1}$.

By comparing the activation energies found from the grain conductivity and the complex polarizability, which were 0.53 eV and 0.11 eV, respectively, it was shown that they were not the same, which means that the conduction process cannot occur by a hopping process.

At low temperatures of 333–373 K, a small number of the charge carriers were thermally active and their movement was not the same, so, the variation of grain conductivity followed variable range hopping (VRH) known as the Mott $[T]^{-1/4}$ law:[22]

$$\sigma = \sigma_1 \exp\left(-\frac{T_0}{T}\right)^{\frac{1}{4}} \qquad (9)$$

where σ_1 is a pre-exponential factor, T_0 is a constant equal to: $\sigma_1 = 6.73 \times 10^{-3}\ \Omega^{-1}\ cm^{-1}$ and $T_0 = 430$ K.

3.4.2. AC conductivity. Fig. 13 shows the variation of $Ln(\sigma_{ac})$ versus $Ln(\omega)$ at different temperatures. It is characterized by the presence of two domains: the first at a high frequency indicating the grain effect, and the second at a low frequency showing the grain boundary effect.

The variation of AC conductivity at high frequencies is marked by the presence of a plateau (σ_0) and a dispersion domain. This evolution follows the Jonscher power law:[23]

$$\sigma_{ac}(\omega) = \sigma_0 + A\omega^{s(T)} \qquad (10)$$

The slope obtained by the fit of the linear part at high frequency of $Ln(\sigma_{ac}) = f(Ln(\omega))$ allowed the determination of the

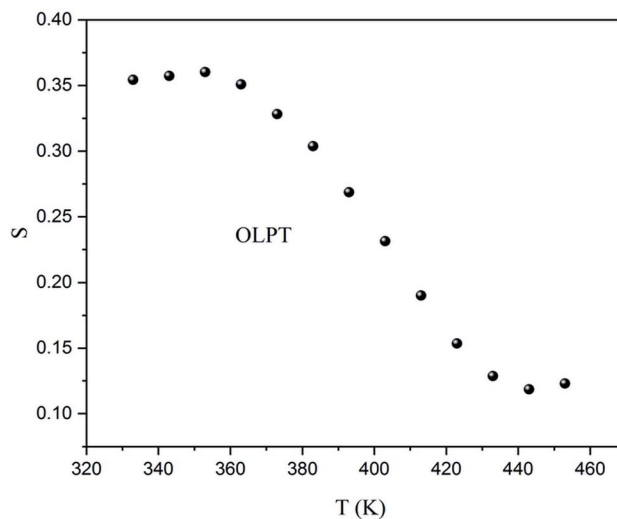'S' exponent which shows the degree of interaction of the mobile ion and its environment. The variation of 'S' as a function of the temperature makes it possible to specify the conduction mechanism in the sample (Fig. 14).

As previously indicated, at low temperatures, the sample was not totally thermally activated, and as a result, the variation as a function of the temperature of 'S' did not give an adequate conduction model. Although, for $T > 360$ K the exponent 'S' decreased when the temperature increased, to give a minimum above 443 K, and then began to increase which meant that the conduction mechanism was overlapping the OLPT.[24]

As the frequency dependence of conductivity is important for investigating the mechanism of conduction, the temperature dependence of conductivity is also important to determine the evolution of the OLPT model. Fig. 15 shows the variation of AC conductivity as function of the inverse of the temperature at
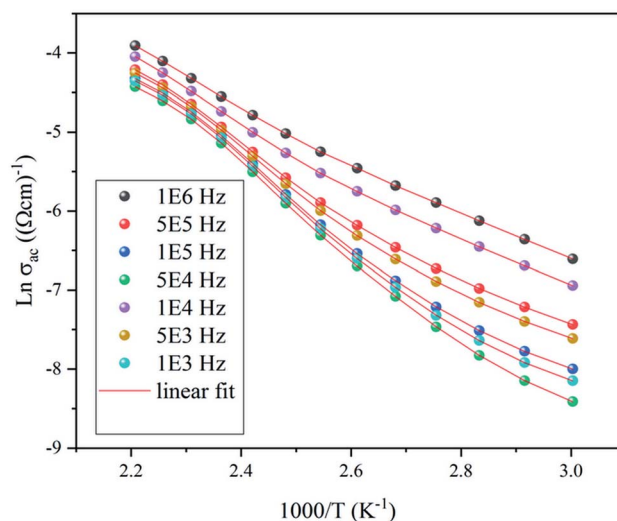

Fig. 15 The variation of $Ln(\sigma_{ac})$ versus $1000/T$.

Table 3 Parameters of the OLPT model

Frequency (10^3 Hz)	N_{EF} (10^{19} eV^{-1} m^{-1})	α (10^9 m^{-1})	W_{H0} (eV)	r_p (Å)
1000	8.6461	3.025	0.485	0.718
500	9.1461	2.490	0.517	0.697
100	9.9728	2.132	0.549	0.716
50	10.293	2.089	0.557	0.738
10	11.794	1.978	0.579	0.785
5	12.004	1.901	0.588	0.823
1	13.756	1.732	0.616	0.935

different frequencies. The good agreement between the experimental data and the theoretical calculation fit proved that the OLPT model described the behavior of the NaCu$_{0.2}$Fe$_{0.3}$Mn$_{0.5}$O$_2$ sample well, enabling an estimation of the parameters according to the equation:[25,26]

$$\sigma(\omega) = \frac{\pi^4}{12} e^2 (K_B T)^2 [N(E_F)]^2 \frac{\omega R_\omega{}^4}{2\alpha K_B T + \left(W_{Ho} r_p / R_\omega{}^2\right)} \quad (11)$$

where r_p is the polaron radius, α is the inverse localization length of the polaron, W_{H0} is the hopping energy of the polaron, $N(E_F)$ is the density of states in the Fermi level, and R_ω is the tunneling distance which could be calculated using eqn (8):

$$R_\omega = \frac{1}{4\alpha} \left[Ln\left(\frac{1}{\omega\tau_0}\right) - \frac{W_{Ho}}{K_B T} \right]$$
$$+ \frac{1}{4\alpha} \left[\left(Ln\left(\frac{1}{\omega\tau_0}\right) - \frac{W_{Ho}}{K_B T}\right)^2 + 8\alpha\frac{W_{Ho}}{K_B T} \right]^{\frac{1}{2}} \quad (12)$$

Table 3 regroups the parameters of the theoretical adjustment of the OLPT model and Fig. 16 displays the variation function of frequency. It was noticed that the density of states decreased with increasing frequency as deduced by Mott law,[27] and also there was a decrease of the polaron radius, and the hopping energy as a function of the frequency was remarkable although this was expected because the decrease in frequency stimulated the mobility of the free charge carriers. It was also noted that the extracted values of R_ω varied over a range of 4 Å, and also with the interatomic spacing (2.384 Å for Na–O and 2.011 Å for Cu, Fe, Mn–O). This finding suggests that the conduction process of these samples, was ensured because of the large polaron. In this case, the spatial extent of the polaron was large when compared with the interatomic distance.[28]

In comparison with other similar compounds such as LiCoO$_2$, which is the most preferred positive electrode material, an improvement of conduction in NaCu$_{0.2}$Fe$_{0.3}$Mn$_{0.5}$O$_2$ was noticed. Indeed, the conductivity of NaCu$_{0.2}$Fe$_{0.3}$Mn$_{0.5}$O$_2$, which
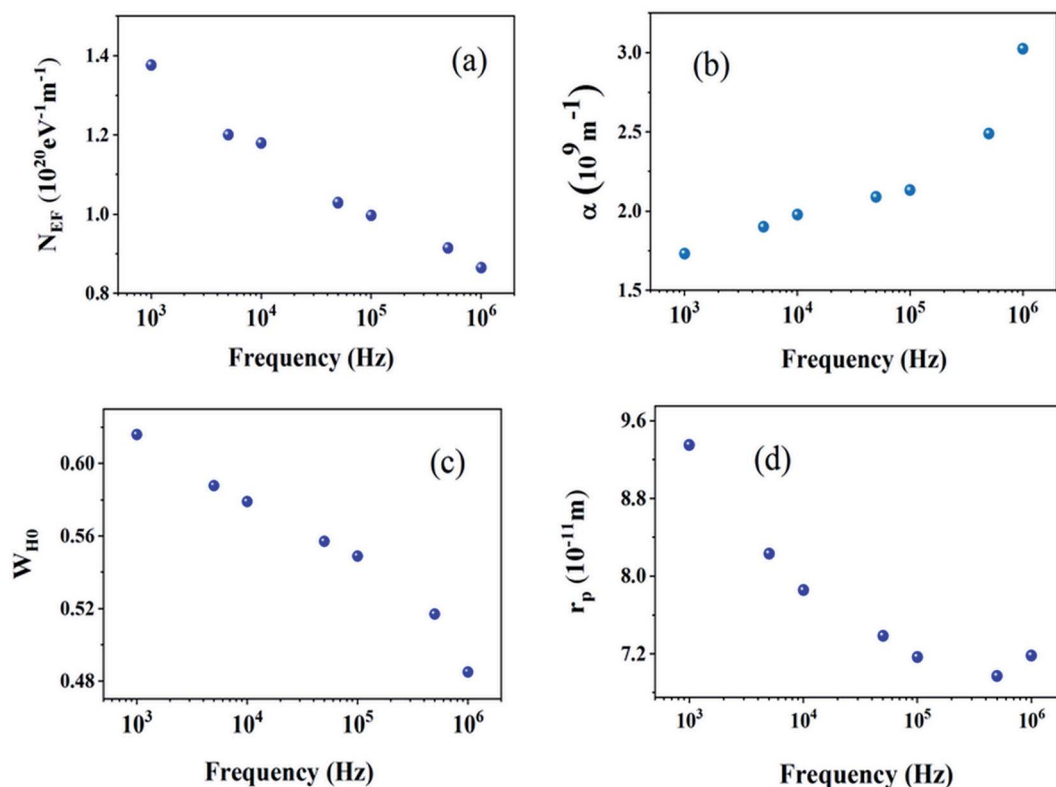

Fig. 16 The variation of the parameters of the OLPT model *versus* the frequency. (a) density of states in the Fermi level, (b) inverse localization lengths of the polaron, (c) the hopping energy of the polaron, and (d) the polaron radius.

is $6 \times 10^{-4} \; \Omega^{-1} \; cm^{-1}$, was greater than that of $LiCoO_2$, which is $2.29 \times 10^{-4} \; \Omega^{-1} \; cm^{-1}$ at room temperature.[29] Therefore, $NaCu_{0.2}Fe_{0.3}Mn_{0.5}O_2$ is a good candidate for Na ion battery applications.

4. Conclusions

The $NaCu_{0.2}Fe_{0.3}Mn_{0.5}O_2$ sample was synthesized *via* a solid-state method. The XRD results prove that this compound crystallizes in a hexagonal system with the $R\bar{3}m$ space group. In addition, optical evaluation indicates that its energy gap is 2.5 eV, which verifies its semiconductor behavior. A dielectric study of this sample was carried out and the polarization phenomena exhibited were due to space charge polarization at low frequency and dipolar polarization at high frequency. The high dielectric constant of $NaCu_{0.2}Fe_{0.3}Mn_{0.5}O_2$ ($10^6 < \varepsilon'_{max} < 10^8$) shows that this material could be a candidate for use in energetic devices. Indeed, materials with a large dielectric constant can be used as dielectric gates or active channels in FET devices. Then, analysis of the complex impedance measurements proves the presence of grain, grain boundary, and electrode effects using Nyquist diagrams. The choice for the adequate equivalent circuit allows for the evaluation of the grain conductivity and shows that the evolution follows the VRH model at a low temperature and the Arrhenius law at a high temperature, with an activation energy of 0.53 eV. The variation of AC conductivity was used to investigate the conduction mechanism, which is the overlapping large polaron tunneling model. In this model the value of the jump distance R_ω is bigger than the interatomic distance and it was seen that the parameters N_{EF}, W_{H0}, and r_p decrease with an increase in frequency. The electrical performance of this material shows that it may be a good candidate for Na-ion battery applications.

Conflicts of interest

There are no conflicts to declare.

References

1 Q. Liu, Z. Hu, M. Chen, C. Zou, H. Jin, S. Wang, S. L. Chou and S. X. Dou, *Small*, 2019, **15**, 1805381.
2 N. Yabuuchi, K. Kubota, M. Dahbi and S. Komaba, *Chem. Rev.*, 2014, **114**, 11636.
3 Y. Xiao, Y. Liu, N. Frederick and F. C. Zhang, *Solid State Ionics*, 2017, **307**, 26.
4 S. Guo, H. Yu, Z. Jian, P. Liu, Y. Zhu, X. Guo, M. Chen, M. Ishida and H. Zhou, *ChemSusChem*, 2014, **7**, 2115.
5 Y. Huang, Y. Zheng, X. Li, F. Adams, W. Luo, Y. Huang and L. Hu, *ACS Energy Lett.*, 2018, **3**, 1604.
6 S. Y. Xu, X. Y. Wu, Y. M. Li, Y.-S. Hu and L. Q. Chen, *Chin. Phys. B*, 2014, **23**, 118202.
7 L. Mu, S. Xu, Y. Li, Y.-S. Hu, H. Li, L. Chen and X. Huang, *Adv. Mater.*, 2015, **27**, 6928.
8 V. Priyanka, A. S. VijaiAnand, K. Mahesh and S. Karpagam, *IOP Conf. Ser.: Mater. Sci. Eng.*, 2017, **263**, 022016.
9 R. Kalthoum, M. Ben Bechir and A. Ben Rhaiem, *Physica E Low Dimens. Syst. Nanostruct.*, 2020, **124**, 114235.
10 A. Jellibi, I. Chaabane and K. Guidara, *Physica E Low Dimens. Syst. Nanostruct.*, 2016, **79**, 167.
11 L. He, Y. Lu, F. Wang, W. Jing, Y. Chen and Y. Liu, *Sens. Actuators,B*, 2018, **254**, 468.
12 A. K. Tangra and G. S. Lotey, *Curr. Appl. Phys.*, 2021, **27**, 103.
13 Y. Xiong, L. Su, X. He, Z. Duan, Z. Zhang, Z. Chen, W. Xie, D. Zhu and Y. Luo, *Sens. Actuators, B*, 2017, **253**, 384.
14 K. Trabelsi, K. Karoui, F. Jomni and A. Ben Rhaiem, *J. Alloys Compd.*, 2021, **867**, 159099.
15 T. Balakrishnan, N. Sankarasubramanian, A. Kavitha and A. Kathalingam, *Mater. Res. Innovations*, 2019, **23**, 216.
16 A. Barhoumi, G. Leroy, B. Duponchel, J. Gest, L. Yang, N. Waldhoff and S. Guermazi, *Superlattice. Microst.*, 2015, **82**, 483.
17 S. Abdul Moyez and S. Roy, *J. Nanoparticle Res.*, 2017, **20**, 5.
18 K. Trabelsi, K. Karoui, A. Mahmoud, J. Bodart, F. Boschini, A. Ben Rhaiem and J. RSC, *Advances*, 2020, **10**, 27456.
19 E. J. Juarez-Perez, R. S. Sanchez, L. Badia, G. Garcia-Belmonte, Y. S. Kang, I. M. Sero and J. Bisquert, *J. Phys. Chem. Lett.*, 2014, **5**, 2390.
20 B. K. P. Scaife, *Proc. Phys. Soc.*, 1963, **81**, 124.
21 A. Ajmi, M. Chemingui, A. Mahmoud, F. Boschini and A. Ben Rhaiem, *Ionics*, 2019, **25**, 1091.
22 N. F. Mott, *J. Non-Cryst. Solids*, 1972, **8**, 1.
23 A. K. Jonscher, *Nature*, 1977, **267**, 673.
24 S. R. Elliott, *Phil. Mag. B*, 1978, **36**, 129.
25 M. Tana, Y. Köseoglu, F. Alana and E. Sentürk, *J. Alloys Compd.*, 2011, **509**, 9399.
26 W. Ben Nasr, H. Kcaou and A. Ben Rhaiem, *Physica E Low Dimens. Syst. Nanostruct.*, 2018, **102**, 110.
27 N. F. Mott and E. A. Davis, *Electronic processes in non-crystalline materials*, Clarendon Press, Oxford, 2nd edn, 1979.
28 S. R. Elliott, *Adv. Phys.*, 1987, **36**, 135.
29 B. Nageswara Rao, M. Venkateswarlu and N. Satyanarayana, *Ionics*, 2014, **20**, 175.